The Astronomical Journal, 145:152 (8pp), 2013 June doi:10.1088/0004-6256/145/6/152

COLOR DEPENDENCE IN THE SIZE DISTRIBUTION OF MAIN BELT ASTEROIDS REVISITED

Tyler M. August and Paul A. Wiegert
Department of Physics and Astronomy, The University of Western Ontario, London, ON N6A 3K7, Canada; tx_august@laurentian.ca
Received 2012 December 21; accepted 2013 April 5; published 2013 May 3

ABSTRACT

The size distribution of the asteroid belt is examined with 16956 main belt asteroids detected in data taken from the Canada–France–Hawaii Telescope Legacy Survey in two filters (g' and r'). The cumulative H (absolute magnitude) distribution is examined in both filters, and both match well to simple power laws down to $H = 17$, with slopes in rough agreement with those reported the literature. This implies that disruptive collisions between asteroids are gravitationally dominated down to at least this size, and probably sub-kilometer scales. The slopes of these distributions appear shallower in the outer belt than the inner belt, and the g' distributions appear slightly steeper than the r'. The slope shallowing in the outer belt may reflect a real compositional difference: the inner asteroid belt has been suggested to consist mostly of stony and/or metallic S-type asteroids, whereas carbonaceous C-types are thought to be more prevalent further from the Sun. No waves are seen in the size distribution above $H = 15$. Since waves are expected to be produced at the transition from gravitationally-dominated to internal strength-dominated collisions, their absence here may imply that the transition occurs at sub-kilometer scales, much smaller than the $H = 17$ (diameter ~ 1.6 km) cutoff of this study.

Key word: minor planets, asteroids: general

Online-only material: color figures

1. INTRODUCTION

The size distribution of the asteroid belt has been an astronomical question since the discovery of 2 Vesta in 1802. The last two hundred years of asteroid hunting have seen the distribution strongly pinned down by observational studies, at least for large objects (see Section 1.1). While the details vary, observations all reveal one characteristic: the number of main belt asteroids (MBAs) rises sharply with decreasing diameter, with the size distribution roughly following a power law. On the theoretical side, it was first shown by Dohnanyi in 1969 that in an ideal steady-state condition, the size distribution should take the form of a power law; in terms of absolute magnitude, H, the cumulative size distribution can be expressed as:

$$\log N(<H) = C + \gamma H \quad (1)$$

where N is the number of objects brighter than H, γ is the slope of the size distribution, and C is its intercept. In the ideal case, $\gamma = 0.5$, (Dohnanyi 1969) but both this predicted slope and the power law itself are based on gross idealizations. For one, the absolute-magnitude distribution only maps simply to actual size if one accepts the (false) assumption that all asteroids are perfect spheres with identical albedo, and size is what drives the collisional physics. Indeed, Dohnanyi (1969) expresses the size distribution in terms of *mass*, which introduces the complication of varying asteroid density as well. Aside from identical, spherical bodies, this power law holds for objects that respond to collisions in a size-independent way (i.e., have the same strength-to-mass ratio at all sizes), which is also untrue of real asteroids. Gravitationally-bound bodies' strength-to-mass ratio increases with size; objects bound by their internal strength have the opposite relation (O'Brien & Greenberg 2003). Nor is the asteroid belt in a steady state: bodies are ground down to ever-smaller sizes and not replaced, and material also leaves the belt through orbital resonances. Instead of an unvarying power law, the main belt is expected to show a depletion of bodies at smaller sizes, which are more fragile per unit mass due to lower gravitational binding energy, and are more quickly removed by Yarkovsky forces. As a result of these removal processes, the ideally featureless power-law slope is expected be superimposed by "waves" of abundance and depletion (Davis et al. 1994; Durda et al. 1998; O'Brien & Greenberg 2003).

In this paper the size distribution of the main belt at sizes down to $H \approx 17$ is measured in two filters, in order to extend our knowledge into the regime $D \sim 1$ km in which internal strength plays an increasingly important role in the bodies' responses to collisions (Farinella et al. 1982; Housen & Holsapple 1990; Benz & Asphaug 1999), and in which compositional differences (possibly indicated by color differences) become increasingly important to asteroid cohesiveness and strength.

1.1. Previous Work

According to Gladman et al. (2009), the belt is almost entirely known below absolute magnitude $H = 15$, and the slope of its cumulative size distribution is $\gamma = 0.5$; there seems a universal agreement that the slope below this point is somewhat lower, but no agreement as to its actual value. The Spacewatch survey (1992–1995), whilst looking for near-Earth objects, found 59,226 MBAs down to a limiting magnitude of $H = 21$ and found $\gamma = 0.36$ below $H = 15$ (Jedicke & Metcalfe 1998). The Sloan Digital Sky Survey, which operated from 1998–2000, mapped the majority of the sky down to magnitude 21.5 in the R band. In the process, they detected ≈13,000 asteroids, and reported $\gamma = 0.26$ below $H = 15$ (Ivezic et al. 2001). The Sub-km Main Belt Asteroid Survey (SMBAS) conducted with the Subaru telescope in 2001 found 1111 asteroids down to a limiting magnitude of 24.4, and reported the size distribution as having $\gamma = 0.24$ for $H \geqslant 18$ (Yoshida et al. 2003). A second run with a different observation sequence, dubbed SMBAS-II, found 1734 asteroids and reported a size distribution of $\gamma = 0.26$ for $H = 19.4$–18 (Yoshida & Nakamura 2007)—it failed to reproduce the differences reported in size distributions in the

inner/middle/outer belts, however. A precursor to this study, Wiegert et al. (2007), also found differing power-law slopes across the belt, along with a marked tendency toward steeper slopes in the r' than g' filters. Section 4.3 is dedicated to comparison with these results. Most recently, the Subkilometer Asteroid Diameter Survey found 1087 asteroids with a size distribution of $\gamma = 0.3$ for $H \geqslant 15$ down to $H \approx 18$ (Gladman et al. 2009). None of the more recent surveys discuss waves in the size distribution, either due to lack of completeness in the $H \geqslant 15$ region or simply because their authors were too preoccupied with determining the slope. Davis et al. (2002) reports a "well known bump" at ≈50–200 km ($H \sim 9.8$–6.8) and the possibility of another from ≈3–30 km ($H \sim 16$–10.8).

2. METHODS

The observations for this work were taken at the Canada–France–Hawaii Telescope (CFHT), a 3.6 m optical/infrared telescope located atop the summit of Mauna Kea in Hawaii. The Canada–France–Hawaii Telescope Legacy Survey (CFHTLS) ran from mid-2003 to early 2009 using more than 2300 hr over 5 yr. The observations supporting this study were taken as part of the "Very Wide" (VW) segment of the CFHTLS, using the 340 megapixel MegaCam instrument, an optical/infrared imager, covering a $1^\circ \times 1^\circ$ FOV (field of view) to a resolution of $0\farcs187$ pixel^{-1}. The VW segment of the CFHTLS covered much of the ecliptic plane (a total area of 410 deg^2) inside a band of ±2 deg. The VW survey was done using MegaPrime g'(400–580 nm), r'(550–700 nm) and i'(670–870 nm) filters. In this study, we neglect the i' component as these images were taken far from opposition, unlike the other two filters. Aside from lowered detection efficiency at a given diameter (due to phase effects) it also proved much more difficult to make accurate orbital estimations for objects imaged in i'. The fields used in the remaining two filters were taken very close to opposition, but at different times and on different nights. As no attempt was made to track asteroids seen in one filter with the other, only a small handful of objects were imaged coincidentally in both. The populations viewed in each filter are thus statistically independent, though similar.

As in Wiegert et al. (2007), the VW survey was chosen for its cadence: the same field was imaged thrice in one night, at ∼45 minute intervals, and once more the following night. MegaCam's large FOV allowed for many successful follow-ups on the second night, which permitted slightly lower uncertainties on the helio- and geocentric distances, and thereby the diameters as well. Images from the CFHTLS were processed with the Elixir pipeline (Magnier & Cuillandre 2004), which includes bias and dark subtraction, flat-fielding, and fringe subtraction. Photometric corrections, including color terms, were computed at this time. The images were then processed by the TERAPIX data-processing center based in Paris for fine astrometric correction to the USNO-B1.0 catalog (Monet et al. 2003). The cleaned images were stored at the Canadian Astronomical Data Centre, from which we retrieved them and began the search for moving objects (Gwyn 2012).

2.1. Detection Protocols

After processing via Elixir and TERAPIX, the first stage of asteroid detection was to use Source Extractor (Bertin & Arnouts 1996) to identify and locate all sources $\geqslant 3\sigma$ above background. Along with position, Source Extractor also provided magnitudes (with photometric corrections from

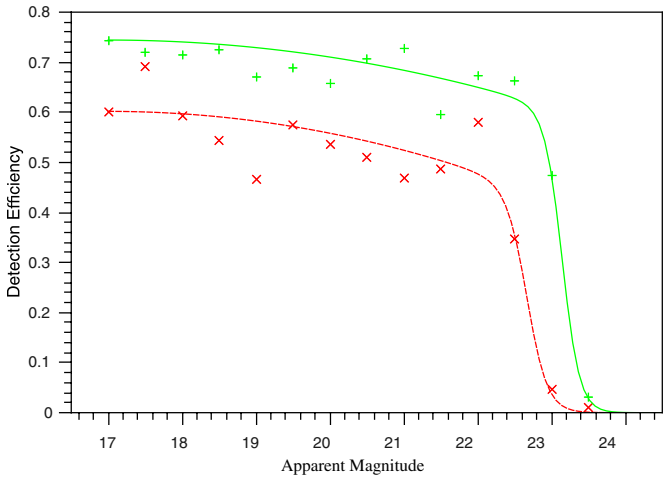

Figure 1. Detection Efficiencies vs. Apparent Magnitude in g' and r' filters. Detection efficiencies estimated for the g' filter are given by green crosses, fitted by a solid line; r' are red x's fitted by a dashed line.

(A color version of this figure is available in the online journal.)

TERAPIX, see above), FWHM, and flags for saturated, overlapping, truncated, and located-on-bad-pixel sources. Stationary sources and obvious cosmic rays were removed by software, and the remaining sources were searched for triplets moving at asteroid-appropriate speeds. These triplets were labeled as asteroid candidates, to be blinked for a human operator. Candidates not clearly asteroidal in appearance (mostly the result of imperfect cosmic ray removal or variations in image quality) were discarded. Remaining objects had preliminary orbits calculated using Väisälä's method (Väisälä 1939; as described in Dubyago 1961), with the assumption that the object was imaged at perihelion. These orbits were projected forward in time in an attempt to recover the object in the next night's image, if the projection remained within the telescope's FOV. If so, the image was blinked to detect an appropriate-magnitude object in the confidence region from Väisälä orbit projection. The final catalogue of one- and two-night detections was analyzed for its size–frequency distribution.

Detection efficiencies (Figure 1) were determined based on a set of artificial calibration sources injected into representative frames taken on randomly selected nights. The artificial sources were implanted moving at typical MBA speeds using the mkobjects function of IRAF (Tody 1986); these objects were then processed as above, including blinking by a human operator. This information was used both to set a detection limit and to debias the data above said limit. Our artificial asteroids are implanted in six different sets of images (three in each g' and r') taken on different nights throughout the CFHTLS survey. The survey covered too many nights to do this effectively on every night. We want to allow a human operator to examine each of the artificial asteroids and thus duplicate our detection procedure as carefully as possible since Petit et al. (2004) noted that the detection efficiency can be overestimated at the faint end if this step is omitted. The price to pay is a reduced number of implanted asteroids and a noisier detection efficiency (500 asteroids were implanted in six images for a total of 3000 objects) but this is smoothed out by the fitting of Equation (2) to the data. The debiasing performed was relatively simple: each detected asteroid was counted as being equivalent to $1/\eta(m_k)$ objects, where $\eta(m_k)$ is the detection efficiency at apparent magnitude m_k in the filter k. Following Gladman et al. (2009), to find $\eta(m_k)$

Table 1
Detection Efficiency Fit Parameters

Filter	η_o	c	m_L	w
g'	0.74	0.0038	23.1	0.12
r'	0.60	0.0048	22.7	0.14

the detection efficiency curves for each filter were fitted by:

$$\eta(m_k) = \frac{\eta_o - c(m_k - 17)^2}{1 + e^{(m_k - m_L)/w}} \quad (2)$$

where η_o is the detection efficiency at $m_k = 17$ and c measures the strength of the quadratic drop, which changes to an exponential falloff of width w near magnitude m_L. The parameters of the fit in each filter are summarized in Table 1. Objects brighter than $m_k = 17$ are considered to have detection efficiency η_o. Our detection efficiency does not reach 100% at brighter magnitudes because of asteroids moving into gaps between the CCD chips. The CFHT MegaCam has a filling factor of 93% (Aune et al. 2003) and asteroids must be observed in all three frames to be detected, so we cannot expect an efficiency above 80%.

Our detection efficiency curves are similar in shape to those of Gladman et al. (2009) and have similar drop-off magnitude m_L and widths w. The main difference is the much lower overall detection efficiency: our $\eta_o < 0.75$ while theirs is about 0.97. This can be traced to the fill factors of the respective detectors. The filling factor of the MegaCam CCD is 93%, which means in any single image there is a .07 probability that the asteroid image will fall into a gap, and a 0.93 probability that it will not. The compound probability that it will not fall into a gap in any of the three images is $0.93^3 = 0.804$, so one cannot expect a detection efficiency above 80% simply due to CCD chip gaps. Though not stated in Gladman et al. (2009), the filling factor of the Kitt Peak National Observatory Mosaic CCD is 99%, and as a result their detection efficiency would be expected to reach $0.99^3 = 0.97$, which is consistent with their Figure 6. Our detection efficiency in r' is also lower than in g' owing to higher sky brightness (and hence more source confusion) in this filter.

3. RESULTS

3.1. The Data and Its Subsets

The data consists of 16,956 asteroid detections in the main belt: 7285 in the g' filter, and 9671 in r'. As discussed in the introduction, the populations imaged in each filter have no appreciable overlap. Thus we cannot segregate based on color as a first-order approximation to spectral type, as done in Yoshida et al. (2003) and Gladman et al. (2009; among others). Just over one-quarter of the asteroid detections could be identified with objects known by the Minor Planet Center (MPC): 3711 in the main belt, of which 1384 were detected in g' and 2327 in r'. While the MPC-linked subset is subject to more complex biases (those of our survey compounded by those of the MPC database) and has poorer statistics than the full survey data set, it has the advantage of much-better orbital data. Instead of arc lengths of one or two days, many of the objects detected in the MPC database have been observed for years—45 oppositions in the case of one object—resulting in much smaller uncertainties on the orbital elements, and the absolute magnitudes thereby. We can use these better-defined orbital elements in an attempt to define our own biases, but due to the complex biases of this subset, we will not examine

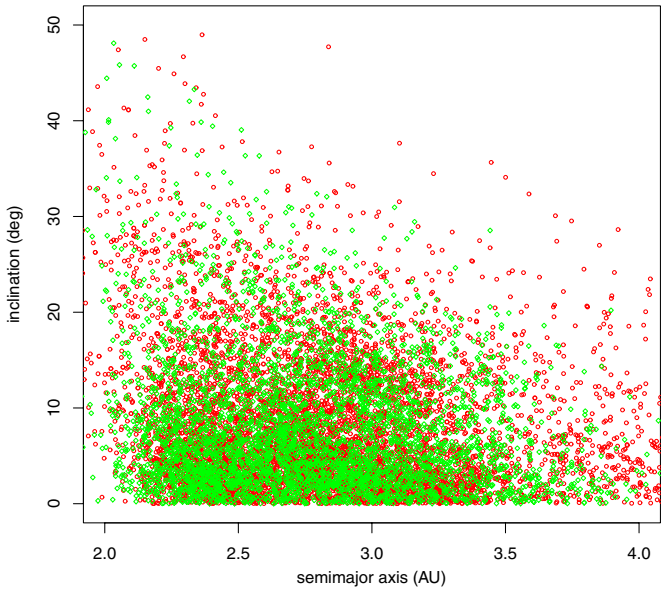

Figure 2. Inclination vs. semimajor axis for all objects observed within the belt. Objects observed in the r' filter are represented by red circles; g', green diamonds. Note the decreasing maximum inclination with semimajor axis, a result of observational bias. Also note the lack of any defining features along the x-axis; the orbital data is not of high enough resolution.

(A color version of this figure is available in the online journal.)

the size distribution of the MPC-linked objects. Following Wiegert et al. (2007), and others, we can also split the data set by semimajor axis, looking for differences between the size distribution in the inner and outer halves of the asteroid belt (Wiegert et al. 2007 split the belt in thirds, but this results in an unacceptable loss of completeness in the innermost bin). This is of special interest due to the compositional gradient across the asteroid belt (stony to carbonaceous, moving outward from the Sun; Cellino 2000). For all size distributions, error bars will be provided by a standard bootstrap process (Efron 1982) based on the uncertainty on the sizes of individual asteroids. Before examining the size distributions, however, it might be a good idea to become better acquainted with the data and its biases.

The orbital elements of each asteroid were calculated from the observations under the assumption of circular orbits by the method of Dubyago (1961). This method produces slightly different results than the method of Herget, which was used in Wiegert et al. (2007), but was chosen for reasons that will be discussed shortly.

Figure 2 shows each object in the full data set plotted by inclination and semimajor axis (as estimated from CFHTLS observations), from 2 to 4 AU. There are a few things to make note of in this plot: one is the sharp cutoff in inclination, which decreases with semimajor axis; this is non-physical and is a bias entirely due to observing geometry and celestial mechanics. One can also note the distinct lack of features along the x-axis: no Kirkwood gaps, and indeed, no firm edge to the asteroid belt out to the Hildas at 4 AU. Due to the short arc lengths, our orbital data is insufficiently precise to resolve these features; it is for this reason that we take the far edge of the asteroid belt at 4 AU rather than the conventional 3.5 AU.

As stated, we can use the MPC-linked subset of the data to illustrate the errors in the remainder of the data. Figures 3 and 4 illustrate differences between orbital elements in the MPC database and those estimated from observations in this

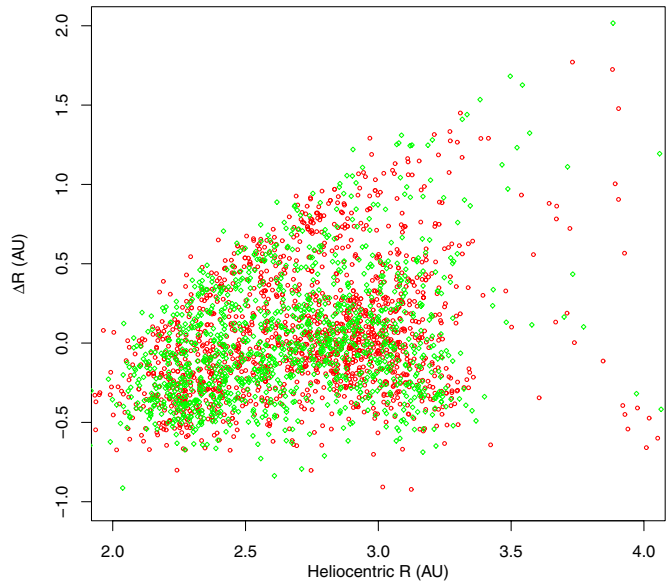

Figure 3. Differences between MPC and observational heliocentric R vs. R. Objects observed in the r' filter are represented by red circles; g', green diamonds.

(A color version of this figure is available in the online journal.)

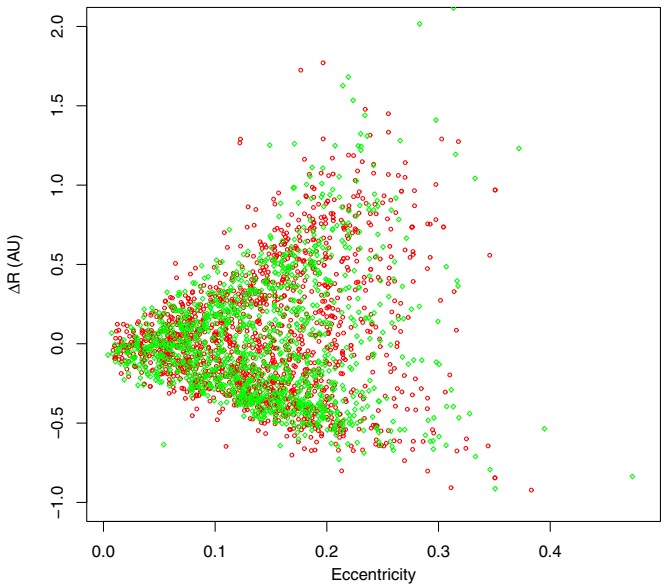

Figure 4. Differences between MPC and observational heliocentric R vs. eccentricity. Objects observed in the r' filter are represented by red circles; g', green diamonds.

(A color version of this figure is available in the online journal.)

survey. The Δx, where x is an orbital element, is defined as $\Delta x \equiv x_{\rm obs} - x_{\rm mpc}$.

Short-arc observations like the ones in this study are subject to systematic errors in the determination of the orbital elements. In particular, since the absolute magnitude H is calculated from

$$H = m - 5\log_{10}(R\Delta) + P(\alpha) \quad (3)$$

where m is apparent magnitude, R is Sun–body distance (AU), Δ is the Earth–body distance, and P is a phase function, which is always less than zero and depends on the phase angle α; any error in R, Δ, or α contributes to error in H. It is worth noting that near opposition, an overestimate in R also overestimates Δ and underestimates α, all three of which act to make the asteroid appear to have a brighter H; all three conspire to produce a fainter H in the reverse case.

Figure 3 shows ΔR (the difference between the R calculated from the asteroid observations and that from the MPC's orbit) versus true R for those asteroids that could be linked via the MPC. The best fit line has a slope of 0.38: clearly we are underestimating the heliocentric distance to asteroids in the inner belt and overestimating it in the outer belt. Ivezic et al. (2001) showed that this was a result of the non-circularities of the asteroid orbits and our data support this conclusion. In Figure 4 we see a plot of ΔR versus eccentricity: larger errors in R are correlated with larger e.

Figure 3 is also the basis for our selection of the Dubyago (1961) orbit determination method mentioned earlier. Three other methods were tested—Herget's (Danby 1989), Moulton–Väisäla–Cunningham (Danby 1989), Väisäla's (Dubyago 1961)—along with Dubyago's (1961). Dubyago's method, which assumes circular orbits, produces the weakest trend in a plot of ΔR versus R. Thus studies of short-arc data could benefit from careful consideration of the orbit determination algorithm and its performance on the particular data set in question.

While in theory it might be possible to use the MPC-linked subset's orbital differences to debias the main data more fully, the MPC database is certainly neither complete nor without bias in this range of magnitudes, and the combined bias of the MPC database and CFHTLS is fairly complex and would need to be investigated in depth. (For example, the reversal of the inclination bias' relationship with semimajor axis). Figure 5 is another example of this, showing the completeness of the two populations—note how much less populated the MPC-linked subset (Figure 5(b)) is at higher magnitudes. The lines marking the 50% detection efficiency limit for the full population have essentially become the limit of completeness in the MPC-linked subset.

Gladman et al. (2009) mention two systematic effects that can affect surveys of our type. The first bias results from using a single cutoff magnitude and taking the detection efficiency to be constant above it. This was done in Wiegert et al. (2007) but here we avoid this issue by adopting the detection efficiency of Equation (2). The second bias is introduced by uncertainties in the heliocentric distance R (as well as Δ and the phase) as a result of the short arcs used here. Our data set certainly includes some systematics of this sort, as can be seen from Figure 3.

The MPC-linked data gives us some idea of the uncertainties in the data. But can we use this knowledge to improve our data set? The Sloan Digital Sky Survey (Ivezic et al. 2001) had data with short arcs ($<$1 day), and used a subset of their data linked to asteroids with well-determined orbit to examine and refine remove trends for their data. We might attempt to do the same by, for example, fitting a line or curve to Figure 3, and using that line or curve to remove the overall trend seen in the figure from our entire sample. This procedure might reduce the average value of ΔR to zero at all R, though some scatter would remain. However we do not know R but only R_o (our calculated heliocentric distance) for our larger sample. A fit based on R_o could be used, but since the difference between R and R_o is largely due to the (unknown) eccentricity, using R_o as a proxy for R is dangerous. Unless the larger sample has the same eccentricity distribution as the MPC-linked sample across the entire belt (possible but not known), new biases may be introduced. We recognize that systematic biases exist within our sample, but have chosen not

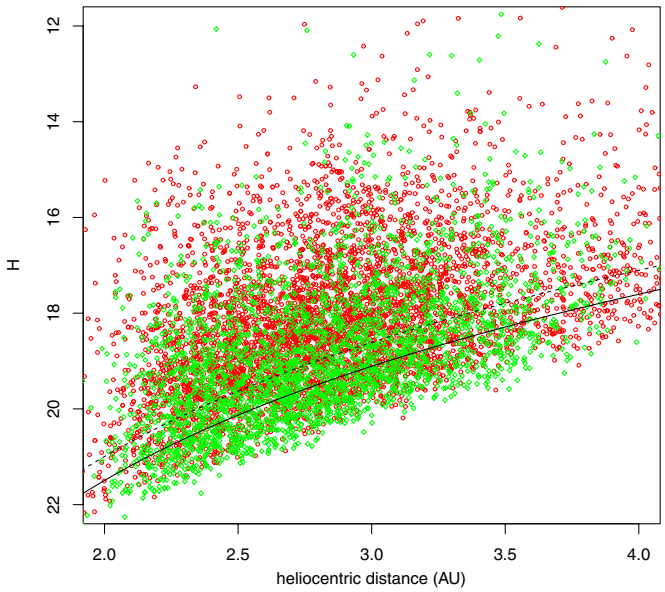

Figure 5. Absolute magnitude vs. heliocentric R for objects in both the full (a) and MPC-linked (b) data sets. Objects observed in the r' filter are represented by red circles; g', green diamonds. The dashed and solid black lines represent the 50% and 90% confidence limits for detection, respectively.

(A color version of this figure is available in the online journal.)

to risk compounding the problem by applying further empirical corrections.

3.1.1. Absolute Magnitude Distributions

Here we present fits in the absolute magnitude distribution that begin at $H_r = 17.1$ and $H_g = 17.6$, corresponding to the 50% normalized detection limit in each filter. Fits are only continued to absolute magnitude $H = 15$, since the size-distribution of the belt is well known below this, and also to avoid the drop-off at low magnitudes where we again lose completeness. The slopes of the fits to the differential distributions are summarized in Table 2. No difference greater than 1σ is observed between filters in either the inner or outer half of the asteroid belt, nor between filters. The differential H distributions are given in Figures 6–8.

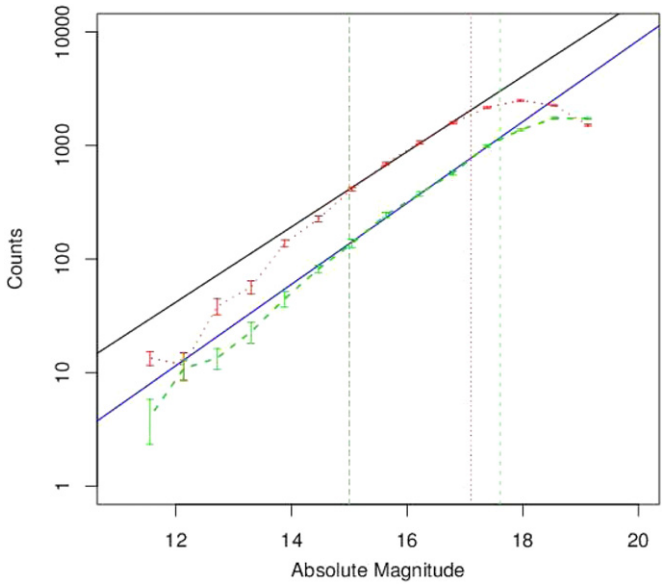

Figure 6. Flux-debiased differential H distribution for the entire asteroid belt ($2\,\mathrm{AU} \leqslant a \leqslant 4$ AU). Dotted red line is the distribution seen in the r' filter; dashed green, g'. The solid lines represent the fit to each filter (r' black, g' blue) and vertical lines indicate the upper and lower limits of the fit in each filter (with the dotted red line corresponding to the r' filter; dashed green, g').

(A color version of this figure is available in the online journal.)

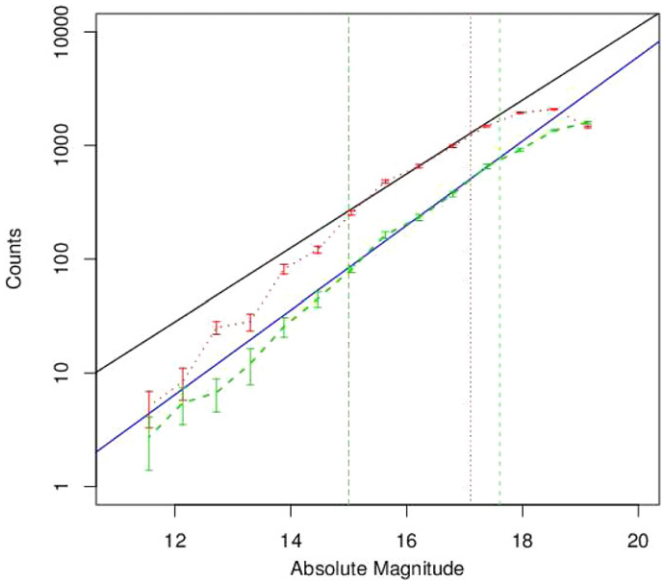

Figure 7. Flux-debiased differential H distribution for the inner asteroid belt ($2\,\mathrm{AU} \leqslant a \leqslant 3$ AU). Dotted red line is the distribution seen in the r' filter; dashed green, g'. The solid lines represent the fit to each filter (r' black, g' blue) and vertical lines indicate the upper and lower limits of the fit in each filter (with the dotted red line corresponding to the r' filter; dashed green, g').

(A color version of this figure is available in the online journal.)

Table 2
Slope of Flux-debiased Differential Absolute Magnitude Distributions

Region	g'	r'
Full Belt	0.3441 ± 0.0108	0.3102 ± 0.0181
Inner	0.3585 ± 0.0188	0.3182 ± 0.022
Outer	0.3383 ± 0.0195	0.3383 ± 0.0324

There are few interesting features on the curves: across the belt, the r' and g' distributions are well behaved and linked closely to its power law from $H = 15$ until loss-of-completeness sets in at high magnitudes. The notable exception is that Figure 8

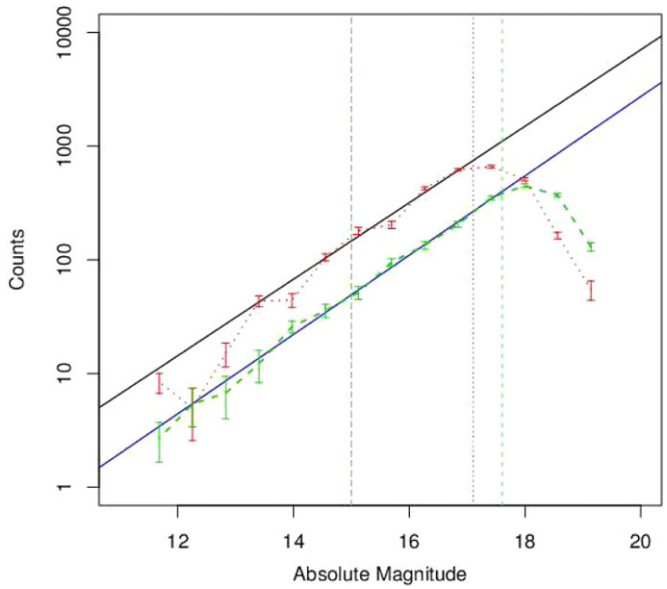

Figure 8. Flux-debiased differential H distribution for the outer asteroid belt ($3\,\mathrm{AU} \leqslant a \leqslant 4\,\mathrm{AU}$). Dotted red line is the distribution seen in the r' filter; dashed green, g'. The solid lines represent the fit to each filter (r' black, g' blue) and vertical lines indicate the upper and lower limits of the fit in each filter (with the dotted red line corresponding to the r' filter; dashed green, g').

(A color version of this figure is available in the online journal.)

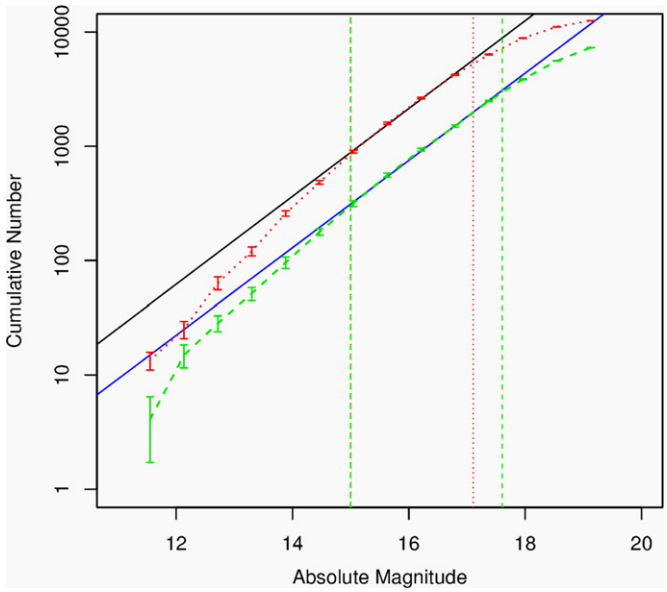

Figure 9. Flux-debiased cumulative H distribution for the entire asteroid belt ($2\,\mathrm{AU} \leqslant a \leqslant 4\,\mathrm{AU}$). Dotted red line is the distribution seen in the r' filter; dashed green, g'. The solid lines represent the fit to each filter (r' black, g' blue) and vertical lines indicate the upper and lower limits of the fit in each filter (with the dotted red line corresponding to the r' filter; dashed green, g').

(A color version of this figure is available in the online journal.)

does show some low-amplitude wavelike action superimposed on the power law in the fitted region. Since they are not reproduced in the cumulative distribution (Figure 11), it is likely that what is being seen is simply noise, which cancels out in the cumulative H distribution (CHD).

Summing up the bins in the differential distributions yields CHDs for the belt as a whole and its two halves. Since there was no discernable difference between debiased and raw-count differential distribution, hereafter only the hopefully-more-accurate flux-debiased counts will be used. The slopes of the power-law fits to the CHDs are given in Table 3. Unlike the differential distribution, there is a statistically discernable difference between the two filters, at least in the outer belt,

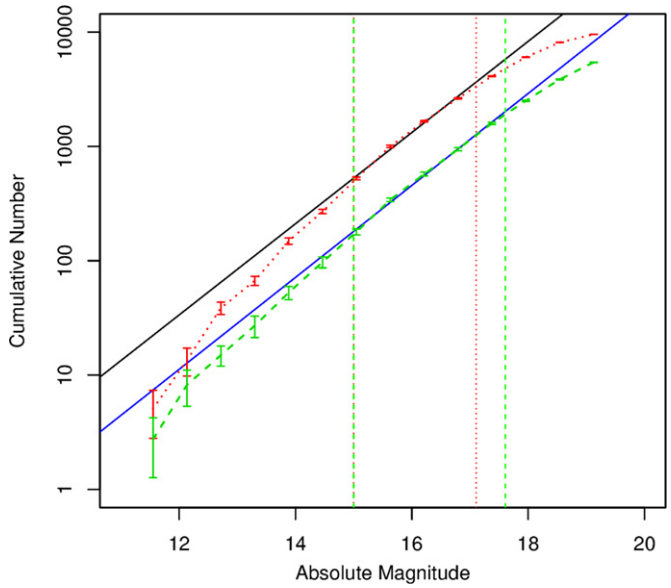

Figure 10. Flux-debiased cumulative H distribution for the inner asteroid belt ($2\,\mathrm{AU} \leqslant a \leqslant 3\,\mathrm{AU}$). Dotted red line is the distribution seen in the r' filter; dashed green, g'. The solid lines represent the fit to each filter (r' black, g' blue) and vertical lines indicate the upper and lower limits of the fit in each filter (with the dotted red line corresponding to the r' filter; dashed green, g').

(A color version of this figure is available in the online journal.)

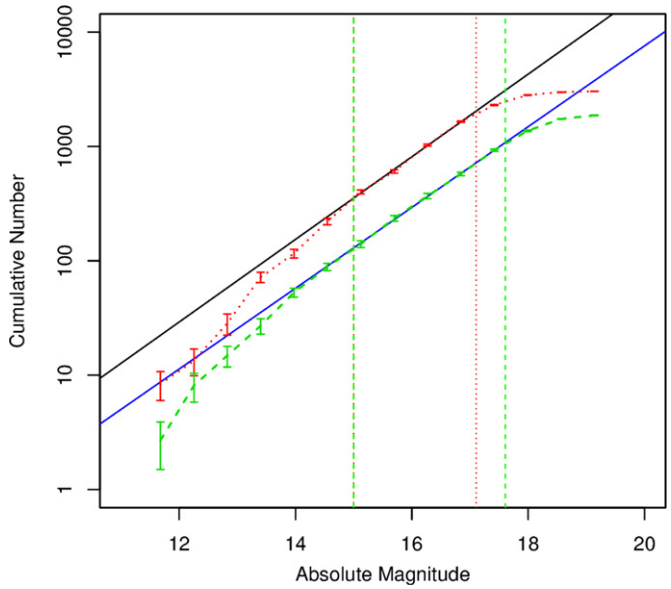

Figure 11. Flux-debiased cumulative H distribution for the outer asteroid belt ($3\,\mathrm{AU} \leqslant a \leqslant 4\,\mathrm{AU}$). Dotted red line is the distribution seen in the r' filter; dashed green, g'. The solid lines represent the fit to each filter (r' black, g' blue) and vertical lines indicate the upper and lower limits of the fit in each filter (with the dotted red line corresponding to the r' filter; dashed green, g').

(A color version of this figure is available in the online journal.)

Table 3
Slope of Flux-debiased Cumulative Absolute Magnitude Distributions

Region	g'	r'
Full Belt	0.3894 ± 0.0104	0.3862 ± 0.0153
Inner Belt	0.3925 ± 0.0178	0.3894 ± 0.0104
Outer Belt	0.3537 ± 0.0055	0.3652 ± 0.0043

where the r' distribution is shallower. Between the inner and outer belt, the r' population also exhibits a detectable shallowing in slope. Looking at the distributions themselves (Figures 9–11), we see that in the fitted region, the distributions are essentially flat across the belt: no waves are observed in either filter, and they match very closely to the fitted power laws.

4. CONCLUSIONS

4.1. Slope of the Size Distributions

The slopes of respective distributions of the full data set are summarized in Tables 2 and 3. The slope of the size distributions all remained constant down to the completeness level, $H_r = 17.1$ and $H_g = 17.6$. We can then conclude that the size-strength transition occurs at smaller scales than this.

The slopes of the size distributions of the populations seen in the g' and r' filters are statistically indistinguishable, except when considering the belt as a whole in the differential distribution, which is steeper in r'. Since the difference is fairly small (1.0σ) and is not reproduced when looking at the cumulative distribution, nor when splitting the belt into two halves in the differential distributions, it is likely that this result is spurious. We therefore conclude there is no real difference between the slopes of the populations imaged in each filter.

There is a little more evidence for a change in slope across the asteroid belt. The r' and g' CHDs show a 1.0σ and 2.6σ shallowing, respectively but no statistically relevant difference is seen in the differential distributions. The average difference of the two g' distributions gives a shallowing with a strength of only 1.5σ; interesting, but not conclusive. It is certainly possible that a shallower slope exists in the outer belt, but is not absolutely clear in this data.

Why might the size distribution appear shallower in the outer belt? It may reflect a real compositional difference: the inner asteroid belt is thought to consist mostly of stony and/or metallic S-type asteroids, whereas carbonaceous C-types are more expected to be prevalent in the outer belt (Gradie & Tedesco 1982). Why this compositional difference would result in an apparent shallowing of the size distribution is not clear. It seems likely that the Yarkovsky effect would act more strongly on the darker, possibly less heat conducting (from meteorites) carbonaceous bodies (Opeil et al. 2010), providing a stronger population sink and thus better-depressing the population at small sizes. This is conjectural, however. Provided the slope difference exists, to test this explanation of it would require orbital simulations that incorporate the compositional gradient of the asteroid belt and the Yarkovsky effect. Better observational data is needed to clarify both the exact nature of any compositional gradient, and the possible gradient in the slope of the size distribution seen here.

The slopes fitted to the size distributions in this study fall within the range given by other studies in the literature, and support the finding in Gladman et al. (2009) that there is no change in slope until sub-kilometer scales.

4.2. Waves in the Size Distributions

There is no compelling evidence for waves in the size distribution at magnitudes fainter than $H = 14$. The only feature that is conclusively present is the bump that appears to occur between the large-scale completeness limit and $H = 14$, and is probably associated with the small-scale bump described in Davis et al. (2002). At smaller scales, there are wavelike features in the differential distributions of both filters, but they do not persist into the cumulative distributions. This is a strong indication that these "wavelike features" are, in fact, the result of random noise that is canceled out by the summation that produces the cumulative distribution. None of the cumulative diameter distributions (see Figures 9–11) show any indication of waves at magnitudes fainter than $H = 15$. The conclusion is that this survey does not show any evidence for any previously unobserved waves in the size distribution. Since waves in the size distribution are a result of the strength–gravitational cohesion slope transition (O'Brien & Greenberg 2003), the discovery of new waves at smaller sizes would have forced a revision of the size at which the transition is expected to occur.

4.3. Comparison with Wiegert et al. (2007)

This study is an extension of the one made in Wiegert et al. (2007); it uses the same survey and the same asteroid-extraction methods, simply on a larger scale; the current study contains $\approx 10\times$ the number of asteroids. There are greater differences in results than one might expect from the improvement in statistics. Notably, Wiegert et al. (2007) reports a significant difference in slope between the r' and g' size distributions. The difference comes down to a better understanding of the data's completeness. Wiegert et al. (2007) attempts to fit the size distribution far lower than it safely can without performing debiasing. Even with flux-based debiasing, this study's small-size cutoff is an order of magnitude larger than theirs (1.6 km versus 0.3 km). In retrospect, we see that having different cut-offs for the g' and r' filters in a region where they are rolling over due to incompleteness is essentially guaranteed to produce differing slopes. As for the knee in the curve, Wiegert et al. (2007) reports it to be at 3.5 km in r' and 2.5 km in g'; but evidently it disappeared under the weight of increased statistics, as there is no evidence for it in the larger data set.

Based on observations obtained with MegaPrime/MegaCam, a joint project of CFHT and CEA/DAPNIA, at the Canada–France–Hawaii Telescope (CFHT), which is operated by the National Research Council (NRC) of Canada, the Institut National des Science de l'Univers of the Centre National de la Recherche Scientifique (CNRS) of France, and the University of Hawaii. This work is based in part on data products produced at the Canadian Astronomy Data Centre as part of the Canada–France–Hawaii Telescope Legacy Survey, a collaborative project of NRC and CNRS. This work was also supported in part by the National Science and Engineering Research Council of Canada.

REFERENCES

Aune, S., Boulade, O., Charlot, X., et al. 2003, Proc. SPIE, 4841, 513
Benz, W., & Asphaug, E. 1999, Icar, 142, 5
Bertin, E., & Arnouts, S. 1996, A&AS, 117, 393
Cellino, A. 2000, SSRv, 92, 397
Danby, J. M. A. 1989, Fundamentals of Celestial Mechanics (Richmond, VA: William-Bell)
Davis, D. R., Durda, D. D., Marzari, F., Campo Bagatin, A., & Gil-Hutton, R. 2002, in Asteroids III, ed. W. F. Bottke, Jr. et al. (Tucson, AZ: Univ. Arizona Press), 545
Davis, D. R., Ryan, E. V., & Farinella, P. 1994, P&SS, 42, 599
Dohnanyi, J. S. 1969, JGR, 74, 2531
Dubyago, A. D. 1961, The Determination of Orbits (New York: MacMillan)
Durda, D. D., Greenberg, R., & Jedicke, R. 1998, Icar, 135, 431
Efron, B. 1982, The Jackknife, the Bootstrap, and Other Resampling Plans (Philadelphia, PA: Society for Industrial and Applied Mathematics)
Farinella, P., Paolicchi, P., & Zappala, V. 1982, Icar, 52, 409

Gladman, B. J., Davis, D. R., Neese, C., et al. 2009, Icar, 202, 104
Gradie, J., & Tedesco, E. 1982, Sci, 216, 1405
Gwyn, S. D. J. 2012, AJ, 143, 38
Housen, K. R., & Holsapple, K. A. 1990, Icar, 84, 226
Ivezic, Z., Tabachnik, S., Rafikov, R., et al. 2001, AJ, 122, 2749
Jedicke, R., & Metcalfe, T. 1998, Icar, 131, 245
Magnier, E. A., & Cuillandre, J. 2004, PASP, 116, 449
Monet, D. G., Levine, S. E., Canzian, B., et al. 2003, AJ, 125, 984
O'Brien, D. P., & Greenberg, R. 2003, Icar, 164, 334
Opeil, C., Consolmagno, G., & Britt, D. 2010, Icar, 208, 449
Petit, J.-M., Holman, M., Scholl, H., Kavelaars, J., & Gladman, B. 2004, MNRAS, 347, 471
Tody, D. 1986, in Proceedings of the Meeting, Instrumentation in Astronomy VI, ed. D. L. Crawford (Bellingham, WA: Society of Photo-Optical Instrumentation Engineers), 733
Väisäla, Y. 1939, Ann. Acad. Sci. Fenn. A, 52, 2 (Astron.-Opt. Inst. Univ. Turku Informo 1)
Wiegert, P., Balam, D., Moss, A., et al. 2007, AJ, 133, 1609
Yoshida, F., & Nakamura, T. 2007, P&SS, 55, 1113
Yoshida, F., Nakamura, T., Watanabe, J.-I., et al. 2003, PASJ, 55, 701